Effect of calcination temperature on structural, magnetic, and dielectric properties of $Mg_{0.75}Zn_{0.25}Al_{0.2}Fe_{1.8}O_4$ ferrites

Tuğba Şaşmaz Kuru[1,*]

[1] *Vocational School of Health Services, İstanbul Okan University, 34959 Istanbul, Turkey*

ABSTRACT

Based on the desire to improve material properties, the effects of temperature have begun to be investigated. It was found that for nano-sized powder materials, such as ferrites, the structural properties like crystal structure and grain size, as well as many magnetic and electrical properties depending on them, change with the calcination temperature. Considering these changes, the effect of calcination temperature on the structural, magnetic, and electrical properties of MZA ferrites ($Mg_{0.75}Zn_{0.25}Al_{0.2}Fe_{1.8}O_4$) prepared by co-precipitation was investigated in this study. The produced MZA ferrites were calcined at three different temperatures (600, 700, and 800 °C). The X-ray diffraction results showed that the samples exhibited a cubic spinel structure. It was found that the crystal sizes (D_sch) calculated using the Debye-Scherrer equation increased with increasing calcination temperature (22.47, 33.53, and 42.53 nm). From the Williamson–Hall (W–H) plots, crystal sizes were calculated almost same as Debye–Scherrer crystal sizes. The nano-sized particles were examined by scanning electron microscope (SEM). Elemental analysis was performed using EDX. v_1 and v_2 absorption bands and O–H and C–H vibrations were detected in the FTIR spectra. Magnetic measurements were carried out at room temperature and in the range of ± 60 kOe under the applied field. Magnetic results are explained by superparamagnetism. Dielectric measurements were performed at room temperature and a frequency range of 20 Hz to 10 MHz. The dielectric properties can be explained by Maxwell–Wagner theory. Impedance spectroscopy study revealed that the relaxation mechanism is consistent with the Cole–Cole model. In AC conductivity studies at room temperature, it was found that the sample calcined at 600 °C would be suitable for energy storage devices.

Springer

1 Introduction

Comparing today's technology with that of the past, a significant size reduction can be observed in almost all areas. The studies focus on nano-sized materials. Numerous properties such as magnetic, electrical, and structural properties make nanoscale materials particularly interesting for certain areas of application. Ferrites, with their unique properties, occupy an important place among nanoscale materials. Ferrites are magnetic materials with a cubic spinel structure [1]. The dielectric and magnetic properties of spinel ferrites play a role in the use of these materials, especially in electronics technology [2]. The general formula of ferrites is MFe_2O_4, and the applications are quite broad and include memory devices, sensor technologies, catalysts, and microwave devices [3, 4]. As a result of intensive studies on ferrite technologies, it has been found that the existing properties of mixed ferrites improve with the substitutions added to the material. As a result, attention has been focused on developing properties with different substitutions. Mg–Zn mixed ferrites are unique materials that many researchers have been working on for decades in various research areas [5–8]. It has the general formula $A_xB_{(1-x)}Fe_2O_4$, where A and B are divalent transition ions, here either Zn or Mg can be present as A or B [9]. Mg–Zn ferrites are superior to other ferrites because of their low cost, mechanical hardness, low dielectric loss, high dielectric constant, and environmental stability [10]. With these features, Mg–Zn ferrites have important application areas such as drug delivery, disease diagnosis, water purification, magnetic recording, and gas and humidity sensors [3, 8, 11].

As with all other ferrites, the properties of Mg–Zn ferrites are strongly influenced by production methods. One of the most effective methods for improving the properties of ferrites is to study the changes in the material obtained by changing the conditions in the ferrite production stages. Numerous methods are used in the production of ferrites, in particular co-precipitation, sol–gel, hydrothermal, and ceramic methods [12–15]. The reason why the co-precipitation method is often preferred is that it offers the possibility to produce under laboratory conditions and its low cost. In addition, the samples obtained have high purity, high homogeneity, and good crystallization.

Substitutions are made to further improve the listed properties of Mg–Zn ferrites. Over the years, various substitutions have been made to Mg–Zn ferrites. These include Mn^{2+}, Ni^{2+}, Y, Cr^{3+}, Sm^{3+}, Sn^{4+} [2, 10, 16–18]. The addition of Al^{+3} to Mg–Zn ferrites increases the softness of the ferrite, which is a desirable property for some high-frequency applications [19, 20]. The addition of Al^{+3} also results in low dielectric and eddy current losses and high resistivity [20]. Because of these properties, Al^{+3} substitution to Mg–Zn ferrites is of interest as it will contribute to technological and scientific developments in the high-frequency range.

Researchers are working to answer the question of how the characteristic properties of materials change when the physical parameters of the materials are altered. It has been studied that the calcination temperature has a positive influence on the material properties of ferrites. The aim of the calcination process is to remove the organic compounds from the sample and ensure the formation of the desired phase [21]. Therefore, calcination processes have begun to be studied to protect the particle integrity and microstructure of nanoscale powders. For most ferrites, the calcination temperature is kept lower than the sintering temperature to increase the activity of the powders [22].

In this study, the change in structural, magnetic, and electrical properties of Al-doped Mg–Zn ferrites ($Mg_{0.75}Zn_{0.25}Al_{0.2}Fe_{1.8}O_4$) at different calcination temperatures was investigated. The samples were prepared by co-precipitation. The product materials were calcined at 600, 700, and 800 °C.

2 Experimental

2.1 Chemicals

Magnesium nitrate ($Mg(NO_3)_2 \cdot 6H_2O$, 99%), zinc nitrate ($Zn(NO_3)_2 \cdot 6H_2O$, 99%), aluminum nitrate ($Al(NO_3)_3 \cdot 9H_2O$, 99%), iron nitrate ($Fe(NO_3)_3 \cdot 6H_2O$, 99%) and Milli-Q ultra-pure water were used as the raw materials in the present work. All the chemicals were purchased from Sigma Aldrich and used without further purification.

2.2 Synthesis of nano ferrites

The fabrication process was carried out as in the author's previous work [4], except for the calcination temperatures of the samples. The template for the nanoparticles is $Mg_{0.75}Zn_{0.25}Al_{0.2}Fe_{1.8}O_4$. According to the fabrication steps in Fig. 1, the calcination temperatures for three
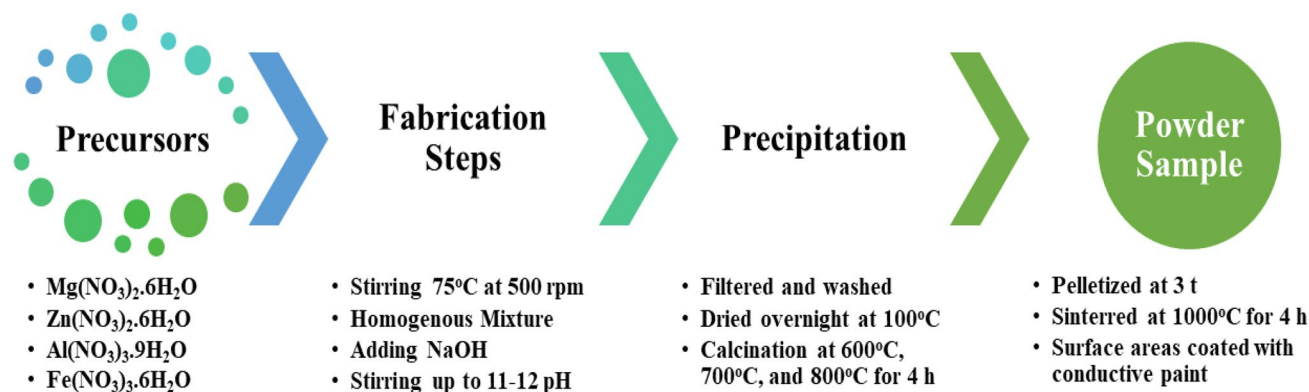
Fig. 1 Fabrication stages

samples are 600, 700, and 800 °C. The samples were labeled as MZA600, MZA700, and MZA800 according to their calcination temperatures.

2.3 Characterization

X-ray diffraction (XRD) analysis for structural characterization and phase formations was performed using the Rigaku Smartlab diffractometer using Cu/Kα ($\lambda = 1.5406$ Å) radiation and 2°/min step width in the 2θ range between 10 and 90°. Morphological and elemental properties of the samples were examined by Scanning Electron Microscopy (SEM, JEOL JSM-7001 F), at an acceleration voltage of 15 kV and Energy-Dispersive X-ray spectroscopy (EDX) technique. Fourier Transform Infrared Spectrometer (FT-IR, Perkin Elmer spectrophotometer) spectra of samples monitored in the range 450–4000 cm^{-1} at room temperature. Magnetic properties of samples were examined using Vibrating Sample Magnetometer by Quantum Design PPMS DynaCool-9 device under applied field in the range of ∓60000 Oe at room temperature. To perform electrical measurements, MZA ferrites in powder form were pelletized under 3 tons of pressure. These pellets were sintered at 1000 °C for 4 h. The surfaces of the pellets were sanded to get rid of roughness and turned into electrodes with silver conductive paint. Dielectric and AC conductivity measurements were performed using LCR Meter (GW Instek, 8110 G) at room temperature and a frequency range of 20 Hz to 10 MHz.

3 Results and discussion

3.1 Structural results

3.1.1 XRD analysis

The synthesized $Mg_{0.75}Zn_{0.25}Al_{0.2}Fe_{1.8}O_4$ nano ferrites were studied by X-ray diffraction method (XRD, Rigaku D/2200P diffractometer) to better understand crystal structure and phase analysis. X-ray diffractometer measurements were performed 2°/min in the range of 2θ = 10–90°, at 40 kV and 30 mA. The XRD results obtained are shown in Fig. 2; Table 1. All three samples have peaks in (220), (311), (400), (422), (511), (440), and (533) planes, which are indicative of the cubic spinel phase (JCPDS 10-0325) [23]. Additional peaks at 24, 49, and 63 degrees exhibit Fe_2O_3 (JCPDS 87-1166) [23]. Looking at the most dominant peak (311), it is observed that the intensity of the peak increases with increasing calcination temperature. We can attribute this increase to the effect of ferrite crystallization with the increase in calcination temperature.

The crystal size was calculated using the Scherrer's formula $D = K\lambda/\cos\theta$, where K is shape factor (0,94), λ is the wavelength of the X-ray, β is the full width at half maximum (FWHM), θ is Bragg angle [24]. Table 1 shows that the crystal size increases with increasing calcination temperature in the range of 22.47–42.53 nm. As the calcination temperature increases, the ionic radii cause thermal oscillations,
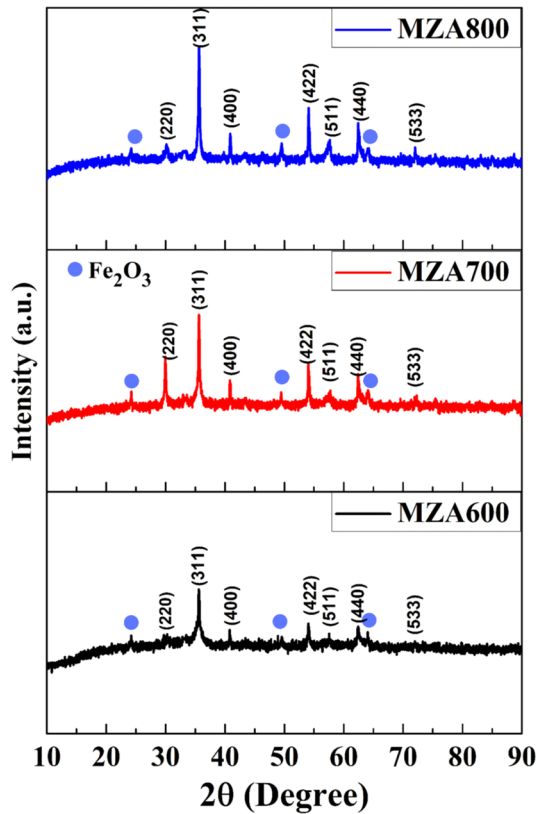
Fig. 2 XRD patterns of MZA samples

leading to an increase in peak intensity and thus crystal size [25]. Another method for determining crystal size is the Williamson–Hall method, which is the simplest of the other methods as it uses the full width at half maximum (FWHM) and the peak angle (θ) of the XRD peaks for the calculation [26]. The strain is also determined using this method. The formula used to draw graphs and determine crystal size and strain in the W–H method is derived as follows:

$$\beta = \beta_{strain} + \beta_f = 4\varepsilon \tan\theta + \frac{K\lambda}{D\cos\theta}, \tag{1}$$

$$\beta\cos\theta = 4\varepsilon\sin\theta + \frac{K\lambda}{D}. \tag{2}$$

Based on the x equation, strain is obtained from the slope of the $\beta\cos\theta - 4\sin\theta$ graph (Fig. 3), while crystal size is calculated from the Y-intercept [27]. The crystal size obtained from the W–H plots increased with the sample order as the calcination temperature increased in the range of 17.48–34.41 nm, similar to that obtained from the Debye–Scherrer equation. Crystal structure strain, which changes with the thermal

and mechanical stresses of the material, gives an idea about the dislocations of the crystal planes; it can be examined as compression strain and tensile strain. Which strain type of the material has been determined from the slope of the W–H plots. While the positive slope is known as tensile strain, the negative slope represents compressive strain [4]. The obtained values are displayed in Table 1. All three samples represented compressive strain as seen in the table.

The lattice parameters a, b, and c are $a = b = c$, since the structure is cubic spinel, and are calculated by the formula $a = d(h^2 + l^2 + k^2)^{1/2}$ using Miller indices [1]. The X-ray and bulk densities were calculated using the formulas $d_x = 8M/Na^3$ and $d_b = m/V$, respectively, and the results are shown in Table 1, where M and N are the molecular weight and Avogadro number. Using the X-ray and bulk densities, the porosity was calculated with the equation $P = (1 - d_b/d_x) \times 100$. Finally, the dislocation density was calculated using the formula $\rho = 1/D_{sch}^2$. The lattice constant decreased with increasing calcination temperature, and the other parameters could be related to the addition of Mg, Zn and Al to Fe, which affects the metal oxidation of Fe [25].

3.1.2 SEM and EDX analysis

Scanning electron microscopy (SEM) is an advanced technique for determining the morphology, crystallography, and topography of nanomaterials. SEM, a type of high-resolution microscope, was used for the in-depth analysis of our samples. The grains and grain boundaries of the synthesized nanomaterials are imaged using SEM. Figure 4 shows SEM images of MZA samples. Clump-like images can be seen in some regions. Due to the magnetic property of iron, agglomeration is observed in most ferrite materials, as in many of our other studies [28]. The agglomerations are largest in sample MZA700 and smallest in sample MZA600. The visible difference in the grain size of each sample is an indication of the influence of annealing temperature on the grain size. It can be said that MZA600 has the more homogeneous grain size among all the samples. There is no doubt that the grains have a nano size despite the agglomerations. Using the ImageJ program, the average particle sizes of 43.744, 48.125, and 58.632 nm determined from the SEM images were calculated for the samples MZA600, MZA700, and MZA800. The effect
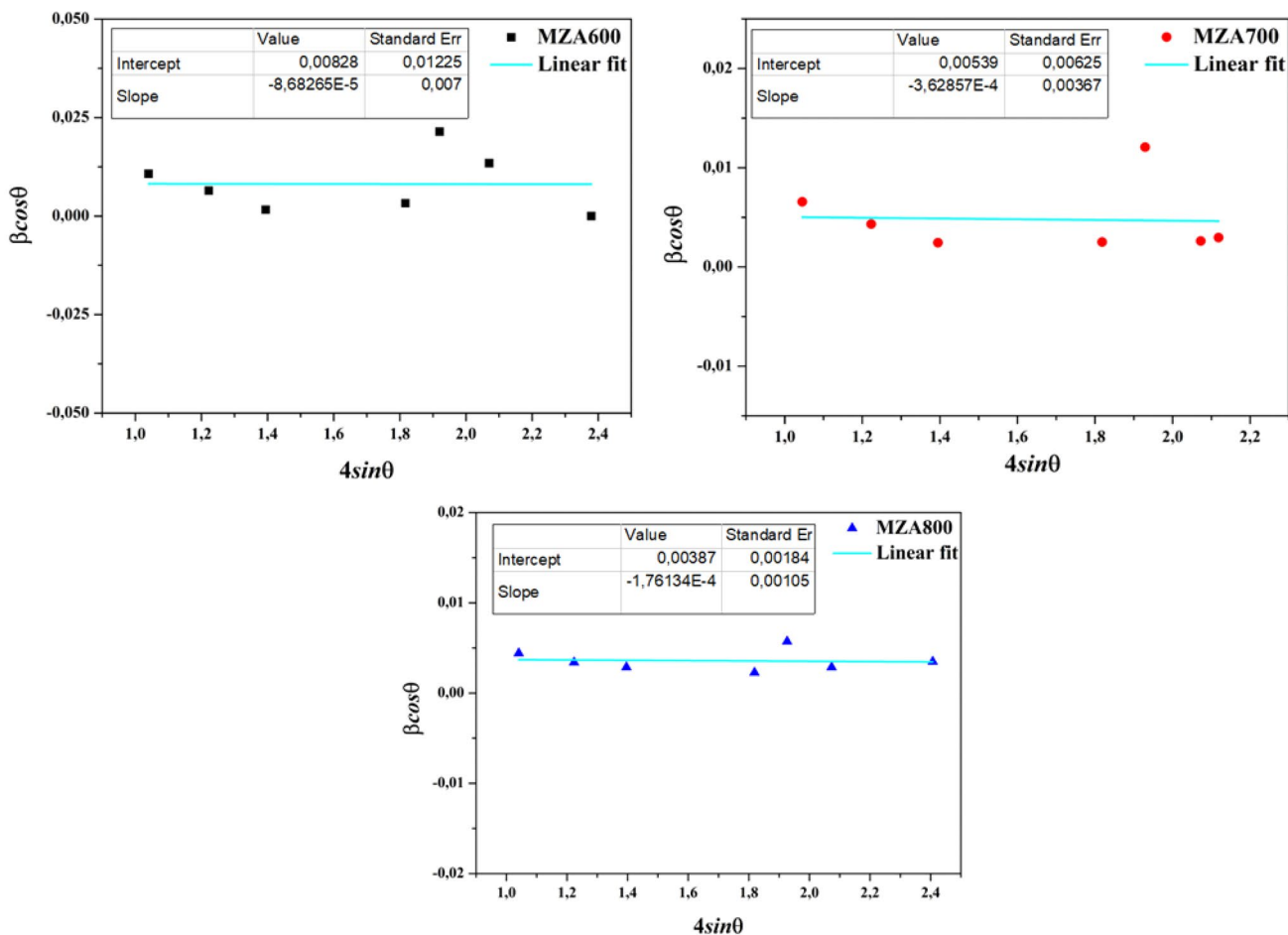
Fig. 3 W–H plots of MZA samples

Table 1 Structural parameters of the MZA samples

	MZA600	MZA700	MZA800
Lattice parameter, a_{exp} (Å)	8.3589	8.3549	8.3519
Debye-Scherrer crystallite size, D_{sch} (nm)	22	34	43
Williamson–Hall crystallite size, D_{W-H} (nm)	17.48	26.86	34.41
X-ray density, $d_x \left(\frac{g}{cm^3} \right)$	4.653	4.659	4.665
Bulk density, $d_b \left(\frac{g}{cm^3} \right)$	4.307	4.327	4.254
Porosity, $P(\%)$	7.44	7.12	8.9
Lattice strain, ε	− 8,68265E-5	− 3,62857E-4	− 1,76134E-4
Dislocation density (ρ)	0.00198	0.000889	0.000553

of calcination temperature on crystal/particle size showed similar results for all three methods (Debye-Scherrer, Williamson–Hall, SEM). However, the average particle size is larger than the crystal size.

The larger particle size is the result of the agglomerations mentioned above as well as grain growth at higher calcination temperature to minimize the Gibbs free energy resulting from the reduction of the large surface area of the nanoparticles [29, 30].
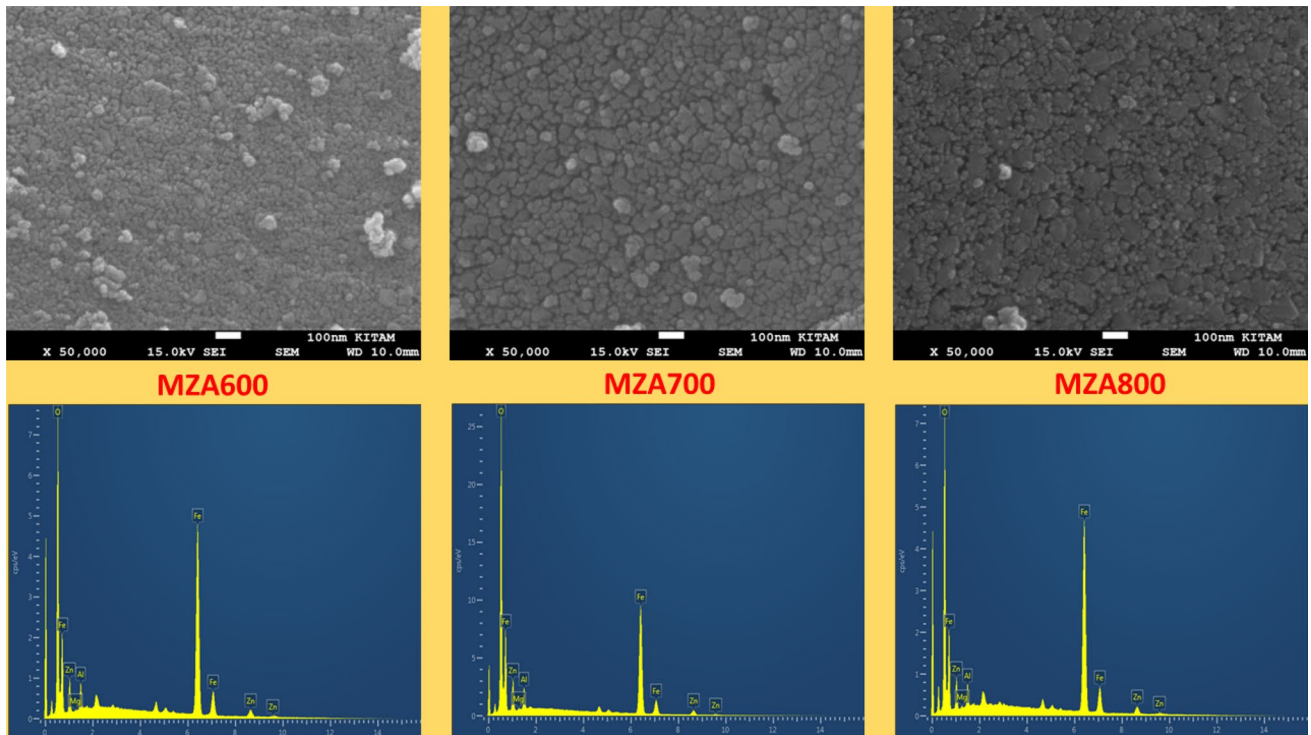
Fig. 4 SEM micrographs and EDX analysis of MZA nano ferrites

Table 2 Calculated and observed at

at.%	Observed			Expected
	MZA600	MZA700	MZA800	
Fe	48.72	47.36	50.13	49.28
O	35.23	34.77	31.71	31.29
Zn	7.56	7.56	7.10	7.99
Al	1.80	2.30	2.46	2.64
Mg	6.69	8.00	8.59	8.80

The elemental analysis of MZA nanoparticles is shown in Fig. 4. Only Mg, Zn, Al, Fe, and O energy peaks are present in the EDX spectrum, and no impurity atoms were found. The percent atomic weights of the samples are indicated in the spectra. Small deviations occurred because the samples were calcined at different temperatures. Calculated and observed at.% values are shown in Table 2.

3.1.3 FT-IR analysis

Fourier transformation inferred technique (FTIR) was studied to obtain information about the emission spectrum by obtaining information on the vibration
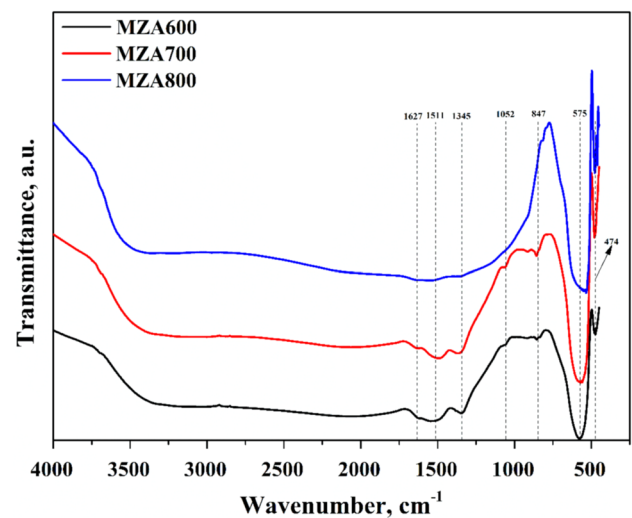

Fig. 5 FT-IR spectra of MZA nano ferrites

mode properties of MZA ferrites. The observed peaks of FTIR spectra of the MZA ferrite samples are presented in Fig. 5. The FTIR measurement was performed in the wavelength range of 450–4000 cm^{-1} to study the bonds and chemical structures of the samples. For all three samples, there are absorption

bands v_1 (~ 575 cm^{-1}) and v_2 (~ 474 cm^{-1}) characteristic of the spinel structure. v_1 denotes Me–O stretching vibrations in tetrahedral regions, v_2 in octahedral regions [31]. The internal lattice vibrations of octahedral and tetrahedral regions are associated with v_1 and v_2 vibration bands [32]. One of the most important features of the FTIR spectrum is that the intensity of the v_1 and v_2 bands differs depending on the fabrication method and fabrication temperature. The small peak at 1627 cm^{-1} and the broad peak at around 3400 cm^{-1} are attributed to the O–H bending and stretching vibrations, which are due to absorbed water molecules and confirm the higher degree of hydration of the co-precipitated samples. The tiny peak at 847 cm^{-1} is the characteristic peak of the spinel ferrites [33]. The peak at 1052 cm^{-1} is attributed to the C–C bending. The peak at about 1511 cm^{-1} indicates stretching vibrations resulting from the absorbed or coordinated Mg/Fe anions [34]. The peak at 1345 cm^{-1} is indicative of the C–H vibrational mode. It is observed that as the calcination temperature increases, the band peaks shift to lower wavelengths. This is due to the grain sizes increase [35]. As a result of the data, we obtained from XRD and SEM results, it is clear that the crystal and particle size increases as the calcination temperature increases. In light of these results, the peak shifts observed in the FTIR graphs can be attributed to grain growth and strain [35]. Along with peak shifts, a decrease in peak intensities and a narrowing in peak broadness are observed with increasing temperature. It can be stated that this decrease in peak intensity and broadness is due to the changing crystal volume as a result of increasing calcination temperature [36].

3.2 Magnetic results

The calcination temperature can significantly affect the structural and magnetic properties of a material. Calcination is the heating of a material at high temperatures, and it usually initiates a chemical reaction that changes the crystal structure and composition of the material. These changes can also affect the magnetic properties of the material. Magnetic properties refer to how a material behaves under the influence of a magnetic field. *M-H* hysteresis loops are a frequently used method for the characterization of magnetic properties. These cycles are plotted as a graph showing how a material's magnetization changes when exposed to a
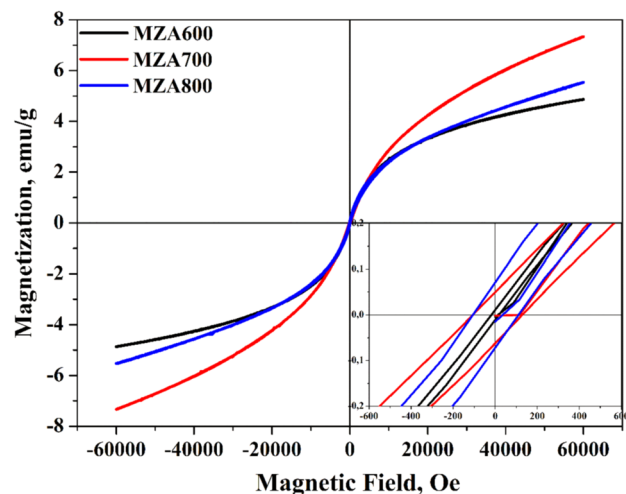

Fig. 6 The room temperature hysteresis loops of MZA nano ferrites

magnetic field. Magnetic hysteresis loops of MZA ferrites are shown in Fig. 6. Measurements were taken at room temperature under an applied field in the range of ± 60 kOe. As can be seen from Fig. 5, all samples calcined at three different temperatures exhibited very narrow hysteresis and "S" shape curves with small coercivity and remanence values, which is a characteristic of superparamagnetic materials [37].

Magnetic properties were determined using this graph and are shown in Table 3. Remanence magnetization (M_r), saturation magnetization (M_s), and coercivity (H_c) values were read from the graph. The squareness ratio (R), anisotropy constant (K), and magnetic moment (μ_B) were then calculated using the following formulas, respectively, based on these values.

$$R = \frac{M_r}{M_s}, \tag{3}$$

$$K = \frac{H_c M_s}{0.96}, \tag{4}$$

$$n_B = \frac{M_{wt} M_s}{5585}, \tag{5}$$

where M_{wt} is the molecular weight.

The magnetic properties of ferrites vary according to their microstructure, annealing temperature, crystal size, chemical composition, production method, and cation distribution [38, 39]. The interaction of

**Table 3** Magnetic properties of the MZA samples

Sample	M_s (emu/g)	M_r (emu/g)	H_c (Oe)	R	K (erg/Oe)	n_B (μ_B)
MZA600	4.86	0.01	17.28	0.002	87.48	0.178
MZA700	7.33	0.05	128.2	0.0068	978.86	0.268
MZA800	5.53	0.07	110.26	0.0126	635.143	0.202

magnetic ions in spinel nanoferrites occurs through AA, BB, or AB interactions between crystal sublattices (tetrahedral (A) and octahedral (B)). In these materials, the magnetic order is strong because it is mediated by oxygen ions in the A and B sublattices [39]. Comparing the magnetic properties of the three samples, MZA700 has the largest saturation magnetization (7.33 emu/g) and coercivity (128.2 Oe). Coercivity and saturation magnetization initially increase after that with the increase of calcination temperature these magnetic parameters decrease. Maximum coercivity values shown in MZA700 can be attributed to the easier domain wall motion than the rotation of magnetization. This behavior of coercivity is the result of single-domain size-induced particle size increase as a result of increasing calcination temperature. When the calcination temperature increased to 800 °C, the coercivity decreased. This is due to the development of the single-domain size limit, resulting in the formation of multiple domains beyond the critical size [30]. Dhaka et al. [40] show that calcination temperature influences the regulation of cation distribution, which affects particle size and magnetization. It shows that the average magnetic field size of the particles of the MZA700 with the highest saturation magnetization is higher than the other samples and the atomic spins are aligned with the direction of the applied magnetic field. It shows that nanoparticles are homogeneously dispersed in lattice structures in samples with small M_r values as given in Table 3. Also, the inter-grain variation in ferrites is determined by the remanence ratio. The squareness ratio of three samples is less than 0.01, indicating that there is magneto-static interaction between samples [41]. Moreover, the fact that the squareness ratio is between 0.01 and 0.1 indicates that the structure of the samples is multi-domain [42]. When the dopant or its amount changes, the difference in the interacting atoms or their amounts causes changes in the magnetic properties. In this study, only the calcination temperature changed while the composition remained the same. Based on this, it can be stated that the changing magnetic properties are affected by the calcination temperature.

3.3 Dielectric characterization

The dielectric constant is a measure of the electrical polarizability of a medium. When electromagnetic waves pass through a dielectric medium, they cause the charges in the medium to move, which causes polarization. This polarization changes the speed, propagation direction, and amplitude of the waves. Contribution to dielectric constant at low frequencies; electronic, ionic, dipolar, and interfacial polarizations [43]. The ε' plots of the samples, plotted against frequency, are shown in Fig. 7. All three samples show the same behavior: As frequency increases, the real dielectric constant decreases until it reaches the MHz range, and then begins to increase. This means that when electromagnetic waves pass through a dielectric medium, the polarization of the charges they accumulate at an earlier point increases up to a certain frequency level, causing the dielectric constant of the medium to decrease. However, at higher frequencies, the limit of polarization enhancement is reached and no further charge can be accumulated. Thereafter, as the frequency increases, the electromagnetic waves
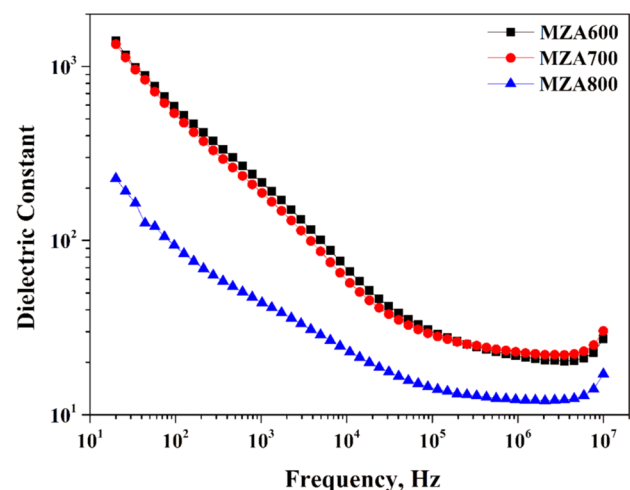
Fig. 7 Frequency dependence of real dielectric constant

have higher energy, accumulating more charge and consequently increasing the value of the dielectric constant. This behavior is typical of many materials, and understanding how the value of the dielectric constant changes with increasing frequency is particularly important for applications such as radio frequency and microwave communications. However, as the calcination temperature increases, the dielectric constant decreases. Calcination temperature is a process in which a material is cooked at high temperatures and often changes the properties of the material. This is due to a decrease in the polarizability of the material. As the calcination temperature increases, the crystals inside the material become better formed and the material becomes denser.

Dielectric loss is usually associated with the dielectric constant. A dielectric material exhibits polarization under the influence of an electric field, meaning that the molecules align in the direction of the electric field and this causes energy loss. Dielectric loss is a result of this energy loss. Dielectric loss is sensitive to variables such as frequency and temperature. For example, at high frequencies, the losses of dielectric materials increase, which is an important factor in applications such as transmission lines and microwave devices. Similarly, as the temperature increases, dielectric loss can also increase, which is a factor to be considered in high-temperature applications. Dielectric loss can affect the insulation properties of a material and can reduce its performance. Therefore, the dielectric loss of a material is an important factor in determining its suitability for an application.
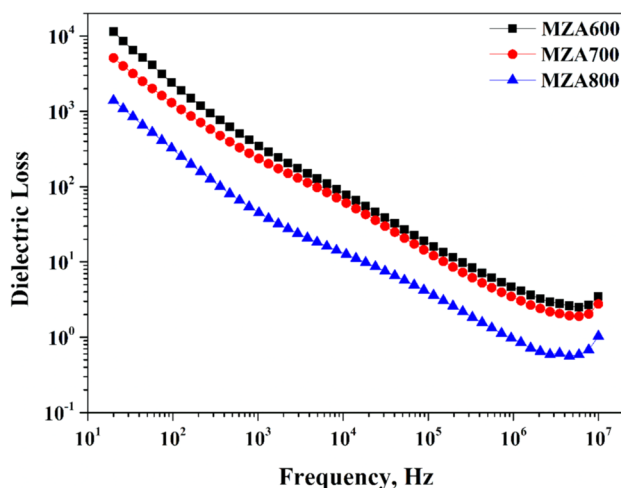
The dielectric loss-frequency curves are shown in Fig. 8. Just like the dielectric constant, dielectric loss also decreases with increasing frequency values. This decrease is a typical dielectric behavior of ferrite materials and is attributed to the Maxwell-Wagner theory and Koops' phenomenon. High-frequency grains cause a small amount of energy demand for electron mobility due to low resistance. Conversely, at low frequencies, energy demand is higher due to high resistance through active grain boundaries [44]. So, while dielectric loss is high at low frequencies, it is lower at high frequencies. It is also possible to observe a decrease in dielectric loss with increasing calcination temperature. This could be the reason for structural variation effects [45]. When we examine the D_{sch} values, it is understood that the crystal size increases as the calcination temperature increases. On the other hand, the dielectric constant and dielectric loss decrease with increasing calcination temperature. Taking into account the contribution of surface charge polarization to the dielectric constant, a larger surface area-to-volume ratio in smaller particles increases the likelihood of surface charges accumulating. Thus, a higher surface charge polarization is created, resulting in a higher dielectric constant [46]. As a result, increasing the calcination temperature leads to larger crystal sizes and lower surface charge polarization. This in turn leads to a decrease in dielectric constant and dielectric losses with increasing calcination temperature.

When we examine the tanθ-frequency variation of the samples (Fig. 9), a decreasing behavior with some fluctuations is observed in all of them with increasing
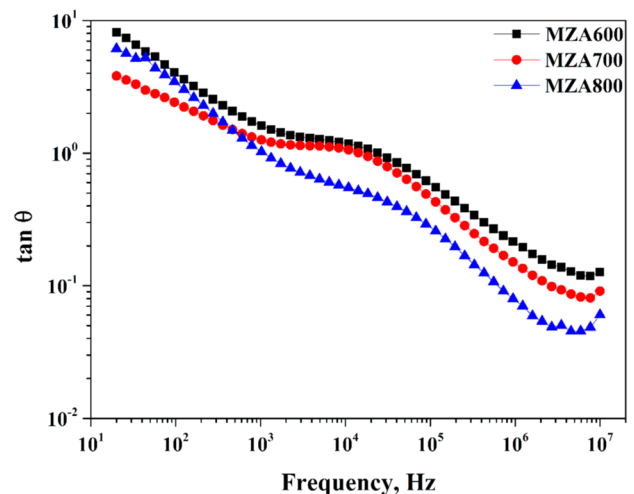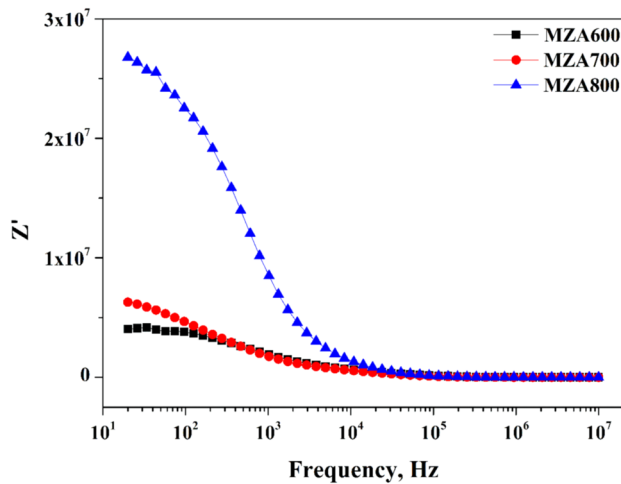

Fig. 8 Frequency dependence of imaginary dielectric constant

Fig. 9 The frequency-dependence of tanθ

Fig. 10 The frequency-dependence of real impedance (Z')
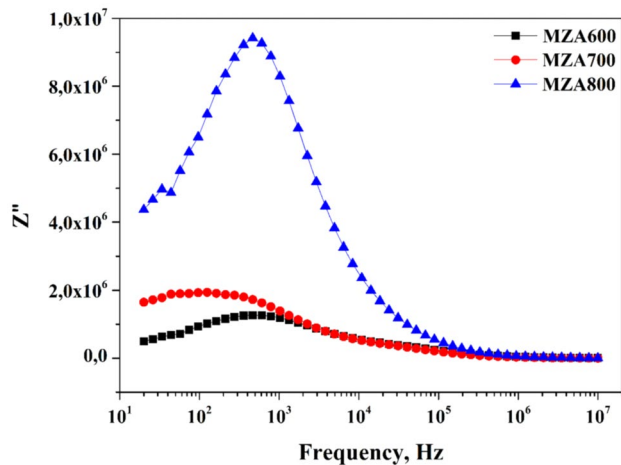
Fig. 11 The frequency-dependence of imaginary impedance (Z'')
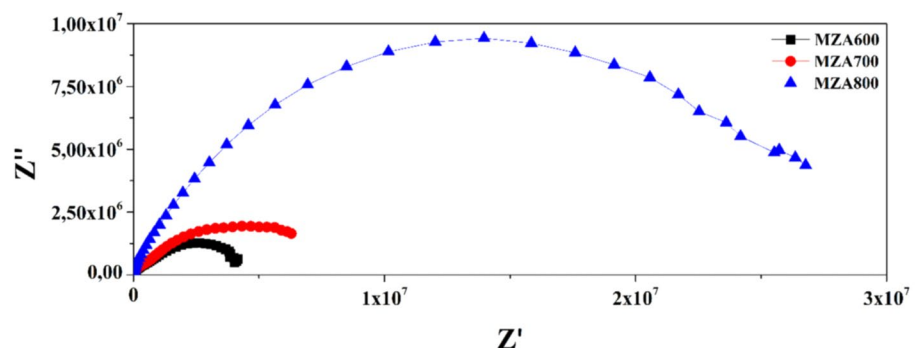
frequency. When the behavior of the samples among themselves is examined separately, it is observed that as the calcination temperature increases, $\tan\theta$ decreases at almost all frequency values. This decrease can be explained by two effects: first, the decrease in porosity causes a decrease in polarization, and second, with the increase in temperature, the increase in Fe^{2+} concentration results in an increase in polarization [47]. Given these circumstances, the mechanism operating in this study can be attributed to the first effect.

3.4 Impedance analysis

Impedance spectra provide information about the conductive and dielectric processes of materials. Graphs that show the change of the real and imaginary parts of impedance with respect to each other are called Nyquist or Cole–Cole plots. The variations of the real and imaginary parts of the impedance with frequency are given in Figs. 10 and 11, respectively.

In Fig. 10, the high Z' value, indicating a continuation of a peak at low frequencies, has been replaced by a frequency-independent behavior at high frequencies. Also in these regions, Z' is independent of calcination temperature. High Z' values at low frequencies are due to low AC conductivity and space charge polarization [39]. As can be seen in the same frequency range, Z' increases with increasing calcination temperature.

Peaks at low frequencies can be seen in the Z''- frequency response in Fig. 11. The peak points can be used to determine the relaxation time of the material. However, these peaks in Z'' are due to the contribution of space charge carriers resulting from oxygen vacancies. Materials consisting of grains and grain boundaries have a high space charge polarization [48]. As with Z'', a decreasing behavior with increasing frequency after the peak point can be seen. In both impedance

Fig. 12 Nyquist plots of nano ferrites

curves, the expected behavior and the behavior we are used to from ferrite materials can be seen. Z' and Z'' both decreasing is not an indicator of an increase in conductivity.

Nyquist plot is shown in Fig. 12. It is clear that there is only one semicircle formed for all samples. Since the centers of the circles are below the x-axis, it can be said that the relaxation mechanism is the Cole–Cole model [49]. An increase in calcination temperature has been observed to increase the diameters of the semicircles. This indicates that differences occurring at grain and grain boundaries due to increasing temperature affect the AC conductivity. The maximum number of semicircles that can be seen in Cole–Cole plots is three, which are formed by grains, grain boundaries, and electrode effects [50]. In this study, the contribution of grains and grain boundaries has resulted in a single semicircle. However, a third semicircle due to electrode effects has not been observed in the impedance spectrum.

3.5 AC conductivity

The conduction mechanism of materials depends on various factors. These factors can be listed as hopping of free charge carriers (electrons and polarons), grain and grain boundaries, mobility of charge carriers, and space charge. The data obtained from the measurements of AC conductivity at room temperature and in the frequency range of 20 Hz to 10 MHz are shown in Fig. 13. The conductivity has increased with increasing frequency and decreased with increasing calcination
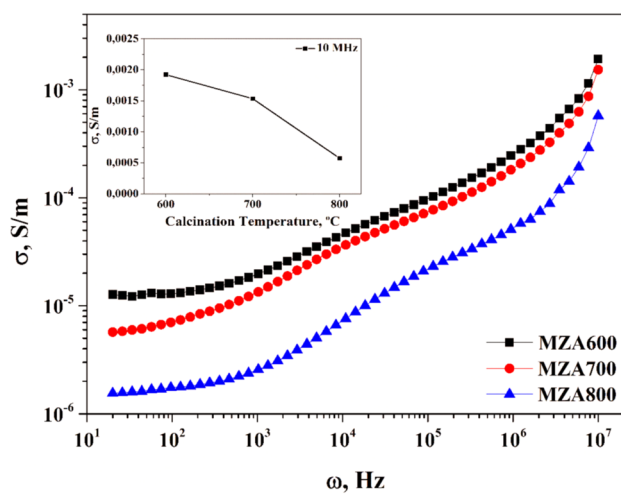
temperature. The increase that occurs with increasing frequency is attributed to the activation of conductive grains as the applied field frequency increases. This will increase the hopping conduction between Fe^{+2} and Fe^{+3} ions and electrons in neighboring octahedral regions [51]. The change depending on frequency can be expressed for ferrite materials with the Maxwell-Wagner theory. The grain boundaries, which are active at low frequencies, give way to more successful grains in terms of conductivity at high frequencies, thus increasing the hopping ability of charge carriers [52]. As the frequency increases, the increase in AC conductivity is consistent with the small-polaron hopping model [51, 53]. AC conductivity decreases with increasing calcination temperature. Compared to the other samples, the increase in conductivity of the sample calcined at 600 °C could make it a good candidate for energy storage devices.

4 Conclusions

Al-doped Mg–Zn ferrite MZA ($Mg_{0.75}Zn_{0.25}Al_{0.2}Fe_{1.8}O_4$) was successfully produced using the co-precipitation method followed by calcination at 600, 700, and 800 °C/4 h. The effect of calcination temperature on the structural, morphological, magnetic, and dielectric properties of MZA ferrite was investigated by XRD, SEM, FTIR, VSM, and dielectric measurements. As the calcination temperature was increased, an increase in the size of crystals and particles was observed, according to the results from XRD, W–H, and SEM analyses. According to the W–H plots, MZA ferrites represent compressive strain. It was observed from the surface morphologies of all samples that the grains were nanosized. Magnetic measurement exhibits superparamagnetic properties. It was understood from the results of frequency-dependent dielectric constant, dielectric loss, impedance, and AC conductivity analysis that the calcination temperature has effects on the dielectric properties of the materials. The effects of grain and grain boundary, which are influenced by changes in calcination temperature, have also changed. The dielectric properties are consistent with the Maxwell-Wagner model. The relaxation mechanism fits the Cole–Cole model. Finally, it was found that the AC conductivity mechanism can be explained by the small-polaron hopping model. With all these results, it has been observed that the structural, magnetic, and

Fig. 13 AC conductivity plots in the various temperatures

electrical properties of MZA ferrites are affected by changing the calcination temperature.

Author contributions

The author took part in conceptualization, methodology, investigation, writing—review, and editing—original draft, validation, and visualization.

Data availability

All data collected for the current study are available in the article.

Declarations

Competing interest The author declares that they have no known competing financial interests or personal relationships that could have appeared to influence the work reported in this paper.

References

1. T.V. Sagar, T. Subba Rao, K. Chandra Babu Naidu, AC-electrical conductivity, magnetic susceptibility, dielectric modulus and impedance studies of sol–gel processed nano-NiMgZn ferrites. Mater. Chem. Phys. **258**, 123902 (2021)

2. U.R. Ghodake, R.C. Kambale, S.S. Suryavanshi, Effect of Mn^{2+} substitution on structural, electrical transport and dielectric properties of Mg–Zn ferrites. Ceram. Int. **43**, 1129–1134 (2017)

3. V. Tukaram, S.S. Shinde, R.B. Borade, A.B. Kadam, Study of cation distribution, structural and electrical properties of Al–Zn substituted Ni–Co ferrite. Phys. B **577**, 411783 (2020)

4. M. Kuru, F. Kılıç Dokan, S. Kuru, Structural, electrical and magnetic characterization of Al^{3+} substituted Mg–Zn ferrites. Appl. Phys. A , 128:286 (2022)

5. D. Ravinder, K. Latha, Dielectric behaviour of mixed Mg–Zn ferrites at low frequencies. Mater. Lett. **41**, 247–253 (1999)

6. M.A. El, Hiti, Dielectric behaviour in Mg-Zn ferrites. J. Magn. Magn. Mater. **192**, 305–313 (1999)

7. B.R. Kumar, D. Ravinder, Dielectric properties of Mn–Zn–Gd ferrites. Mater. Lett. **53**, 437–440 (2002)

8. S. Ghatak, M. Sinha, A.K. Meikap, S.K. Pradhan, Alternate current conductivity and dielectric properties of non-stoichiometric nanocrystalline Mg–Zn ferrite below room temperature. Phys. E. **42**, 1397–1405 (2010)

9. M.A. Rahman, M.T. Islam, M.S.J. Singh, M. Samsuzzaman, M.E. Chowdhury, Synthesis and characterization of Mg–Zn ferrite based flexible microwave composites and its application as SNG metamaterial. Sci. Rep. **11**, 7654 (2021)

10. M.A. Ali, M.N.I. Khan, F.U.Z. Chowdhury, M.M. Hossain, S.M. Hoque, M.M. Uddin, Impact of Sn^{4+} substitution in Mg–Zn ferrites: deciphering the structural, morphological, dielectric, electrical and magnetic properties. Mater. Chem. Phys. **263**, 124357 (2021)

11. A. Gholizadeh, M. Beyranvand, Investigation on the structural, magnetic, dielectric and impedance analysis of Mg0.3-xBaxCu0.2Zn0.5Fe2O4 nanoparticles. Phys. B **584**, 412079 (2020)

12. K. Verma, A. Kumar, D. Varshney, Dielectric relaxation behavior of $A_xCo_{1-x}Fe_2O_4$ (A = zn, mg) mixed ferrites. J. Alloys Compd. **526**, 91–97 (2012)

13. E. Şentürk, Y. Köseoğlu, T. Şaşmaz, F. Alan, M. Tan, RC circuit and conductivity properties of $Mn_{0.6}Co_{0.4}Fe_2O_4$ nanocomposite synthesized by hydrothermal method. J. Alloys Compd. **578**, 90–95 (2013)

14. S.B. Patil, R.P. Patil, J.S. Ghodake, B.K. Chougule, Temperature and frequency dependent dielectric properties of Ni–Mg–Zn–Co ferrites. J. Magn. Magn. Mater. **350**, 179–182 (2014)

15. S. Soreto Teixeira, A.J.M. Sales, M.P.F. Graça, L.C. Costa, Yttrium ferrites with enhanced dielectric properties. Mater. Sci. Eng. B **232**, 41–47 (2018)

16. E. Melagiriyappa, H.S. Jayanna, B.K. Chougule, Dielectric behavior and ac electrical conductivity study of Sm^{3+} substituted Mg–Zn ferrites. Mater. Chem. Phys. **112**, 68–73 (2008)

17. D.H. Bobade, S.M. Rathod, M.L. Mane, Sol–gel auto-combustion synthesis, structural and enhanced magnetic properties of Ni^{2+} substituted nanocrystalline Mg–Zn. Spinel Ferrite Phys. B **407**, 3700–3704 (2012)

18. M.A. Ali, M.N.I. Khan, F.-U.-Z. Chowdhury, M.M. Hossain, M.Z. Rahaman, S.M. Hoque, M.A. Matin, M.M. Uddin, Study of physical properties towards optimizing sintering temperature of Y substituted Mg–Zn ferrites. Results Phys. **14**, 4–5 (2019)

19. A. Lassoued, M.S. Lassoued, B. Dkhil, S. Ammar, A. Gadri, Substituted effect of Al^{3+} on structural, optical, magnetic and photocatalytic activity of Ni ferrites. J. Magn. Magn. Mater. **476**, 124–133 (2019)

20. M.Z. Khan, I.H. Gul, M.M. Baig, A.N. Khan, Comprehensive study on structural, electrical, magnetic and photocatalytic degradation properties of Al^{3+} ions substituted nickel ferrites nanoparticles. J. Alloys Compd. **848**, 155795 (2020)

21. R.B. Assis, M.R.D. Bomio, R.M. Nascimento, C.A. Paskocimas, E. Longo, F.V. Motta, Rapid calcination of ferrite $Ni_{0.75}Zn_{0.25}Fe_2O_4$ by microwave energy. J. Therm. Anal. Calorim. **118**, 277–285 (2014)

22. H. Su, H. Zhang, X. Tang, Z. Zhong, F. Bai, Influences of high calcination temperature on densification and magnetic properties of low-temperature-fired NiCuZn ferrites. IEEE Trans. Magn. **47**, 4328–4331 (2011)

23. H.M. Zaki, S.H. Al-Heniti, T.A. Elmosalami, Structural, magnetic and dielectric studies of copper substituted nanocrystalline spinel magnesium zinc ferrite. J. Alloys Compd. **633**, 104–114 (2015)

24. S.K. Abdel-Aal, M.F. Kandeel, A.F. El-Sherif, A.S. Abdel-Rahman, Synthesis, characterization, and Optical properties of New Organic–Inorganic Hybrid perovskites $[(NH_3)_2(CH_2)_3]CuCl_4$ and $[(NH_3)_2(CH_2)_4]CuCl_2Br_2$. Phys. Status Solidi A **218**, 2100036 (2021)

25. A.M.S. Sebayang, L.P.S. Sagala, P. Sinuhaji, N.S. Asri, A.P. Tetuko, E.A. Setiadi, L.F. Nurdiansyah, M. Ginting, P. Sebayang, M. Hamid, M. Rianna, Enhanced calcination temperatures of $Zn_{0.6}Ni_{0.2}Cu_{0.2}Fe_2O_4$ on thermal,

26. K.R. Desai, S.T. Alone, S.R. Wadgane, S.E. Shirsath, M. Khalid, A. Batoo, E.H. Imran, M. Raslan, M.F. Hadi, R.H. Ijaz, Kadam, X-ray diffraction based Williamson–Hall analysis and rietveld refinement for strain mechanism in Mg–Mn co-substituted $CdFe_2O_4$ nanoparticles. Phys. B **614**, 413054 (2021)

27. S.K. Abdel-Aal, A.S. Abdel-Rahman, Graphene influence on the structure, magnetic, and optical properties of rare-earth perovskite. J. Nanopart. Res. **22**, 267 (2020)

28. T. Şaşmaz Kuru, V. Eyüpoğlu, F. Yıldız, The effect of Al^{3+} additive on the structural, optical, and magnetic properties of Al–Cd ferrites fabricated by coprecipitation method. Acta Phys. Polonica A **134**, 1092–1098 (2018)

29. K.H. Maria, U.S. Akther, I.N. Esha, M.S. Hossain, M.N.I. Khan, Estimation of structural, electrical, and magnetic variations of Mn-Ni- Zn ferrites by substituting rare earth Y^{3+} for high-frequency applications. J. Supercond. Novel Magn. **33**, 2133–2142 (2020)

30. M. Basak, M.L. Rahman, M.F. Ahmed, B. Biswas, N. Sharmin, Calcination effect on structural, morphological and magnetic properties of nano-sized $CoFe_2O_4$ developed by a simple co-precipitation technique. Mater. Chem. Phys. **264**, 124442 (2021)

31. E. Petrova, D. Kotsikau, V. Pankov, A. Fahmi, Influence of synthesis methods on structural and magnetic characteristics of Mg–Zn-ferrite nanopowders. J. Magn. Magn. Mater. **473**, 85–91 (2019)

32. C.V. Reddy, S.V.P. Vattikuti, R.V.S.S.N. Ravikumar, S.J. Moon, J. Shim, Influence of calcination temperature on $Cd_{0.3}Co_{0.7}Fe_2O_4$ nanoparticles: structural, thermal and magnetic properties. J. Magn. Magn. Mater. **394**, 70–76 (2015)

33. C.V. Reddy, C. Byon, B. Narendra, B. Dudem, J. Shim, S.J. Moon, P. Vattikuti, Effect of calcination temperature on cobalt substituted cadmium ferrite nanoparticles. J. Mater. Sci. Mater. Electron. **26**, 5078–5084 (2015)

34. G. Dhillon, N. Kumar, M. Chitkara, I. Singh Sandhu, Effect of A-site substitution and calcination temperature in Fe_3O_4 spinel ferrites. J. Mater. Sci: Mater. Electron. **31**, 18903–18912 (2020)

35. E. Rezaie, A. Rezanezhad, L.S. Ghadimi, A. Hajalilou, N. Arsalani, Effect of calcination on structural and supercapacitance properties of hydrothermally synthesized plate-like $SrFe_{12}O_{19}$ hexaferrite nanoparticles. Ceram. Int. **44**, 20285–20290 (2018)

36. R. Verma, A. Chauhan, K. Neha, R. Mujasam Batoo, M. Kumar, E.H. Hadhi, Effect of calcination temperature on

structural and morphological properties of bismuth ferrite nanoparticles. Ceram. Int. **47**, 3680–3691 (2021)

37. M. Chand, A. Kumar, S. Kumar, A. Shankar, R.P. Pant, Investigations on $Mn_xZn_{1-x}Fe_2O_4$ (x = 0.1, 0.3 and 0.5) nanoparticles synthesized by sol–gel and co-precipitation methods. Indian J. Eng. Mater. Sci. **18**, 385–389 (2011)

38. S.F. Mansour, M.A. Abdo, S.M. Alwan, The role of Cr^{3+} ions substitution on structural, magnetic and dielectric modulus of manganese zinc nanoferrites. Ceram. Int. **44**, 8035–8042 (2018)

39. A. Rajeshwari, I.K. Punithavathy, S.J. Jeyakumar, M. Jothibas, S.A. Kumar, $CoGd_xFe_{2-x}O_4$ (0.00 ≤ x ≥ 0.08) nanoferrites: effect of Gd^{3+} ions on structural, optical, magnetic, and dielectric properties. J. Mater. Sci. Mater. Electron. **33**, 5953–5969 (2022)

40. S. Dhaka, S. Kumar, K. Poonia, Effect of annealing temperature on structural and magnetic properties of nano-cobalt ferrite. J. Mater. Sci. Mater. Electron. **32**, 16392–16399 (2021)

41. Z.L. Wang, Y. Liu, Z. Zhang, *Handbook of nanophase and nanostructured materials. materials systems and applications I*, vol. 3 (Kluwer, New York, 2003)

42. H.N. Chaudhari, P.N. Dhruv, C. Singh, S. Singh Meena, S. Kavita, R.B. Jotania, Effect of heating temperature on structural, magnetic, and dielectric properties of magnesium ferrites prepared in the presence of *Solanum Lycopersicum* fruit extract. J. Mater. Sci. Mater. Electron. **31**, 18445–18463 (2020)

43. J.C.R. Araújo, S. Araujo-Barbosa, A.L.R. Souza, C.A.M. Iglesias, J. Xavier, P.B. Souza, C.C. Pl´a Cid, S. Azevedo, R.B. da Silva, M.A. Correa, S.N. de Medeiros, E.F. Silva, F. Bohn, Tuning structural, magnetic, electrical, and dielectric properties of $MgFe_2O_4$ synthesized by sol-gel followed by heat treatment. J. Phys. Chem. Solids. **154**, 110051 (2021)

44. A.M. Mohammad, S.M.A. Ridha, T.H. Mubarak, Dielectric properties of Cr-substituted cobalt ferrite nanoparticles synthesis by citrate-gel auto combustion method. Int. J. Appl. Eng. **13**, 6026–6035 (2018)

45. P. Bhavani, N.R. Reddy, I.V.S. Reddy, M. Sakar, Manipulation over phase transformation in iron oxide nanoparticles via calcination temperature and their effect on magnetic and dielectric properties. IEEE Trans. Magn. **53**, 1–5 (2017)

46. E. Ranjith Kumar, C. Srinivas, M. Deepty, I. Pradeep, M.V.K. Mehar, C.L. Prajapat, T.V. Chandrasekhar Rao, N. Krishna Mohan, D.L. Sastry, Synergistic effect of heat treatment on structural, magnetic and dielectric properties of spinel ferrite nanoparticles. J. Mater. Sci. Mater. Electron. **29**, 20968–20977 (2018)

47. H. Huili, B. Grindi, A. Kouki, G. Viau, L. Ben Tahar, Effect of sintering conditions on the structural, electrical, and magnetic properties of nanosized $Co_{0.2}Ni_{0.3}Zn_{0.5}Fe_2O_4$. Ceram. Int. **41**, 6212–6225 (2015)

48. M. Kuru, T. Şaşmaz, Kuru, temperature- and frequency-dependent electrical characterization with humidity properties in MZC nanoferrites. J. Mater. Sci. Mater. Electron. **33**, 18587–18606 (2022)

49. E. Mccafferty, On the determination of distributed double-layer capacitances from cole–cole plots. Corros. Sci. **39**, 243–254 (1997)

50. M.M. Hossen, M. Belal Hossen, Structural, electrical and magnetic properties of $Ni_{0.5}Cu_{0.2}Cd_{0.3}La_xFe_{2-x}O_4$ nanoferrites due to lanthanum doping in the place of trivalent iron. Phys. B Phys. Condens. Matter **585**, 412116 (2020)

51. K. Akhtar, M. Gul, I.U. Haq, S.S.A. Shah, Z.U. Khan, Effect of calcination temperature on the morphological and dielectric properties of phase-pure $MnCrFeO_4$ nanoparticles. Inorg. Nano Metal Chem. **47**, 1722–1727 (2017)

52. Mubasher, M. Mumtaz, M. Hassan, L. Ali, Z. Ahmad, M.A. Imtiaz, M.F. Aamir, A. Rehman, K. Nadeem, Comparative study of frequency–dependent dielectric properties of ferrites MFe_2O_4 (M = co, mg, cr and mn) nanoparticles. Appl. Phys. A **126**, 334 (2020)

53. T. Şaşmaz Kuru, M. Kuru, S. Bağcı, Dielectric, humidity behavior and conductivity mechanism of $Mn_{0.2}Ni_{0.3}Zn_{0.5}Fe_2O_4$ ferrite prepared by co-precipitation method. J. Mater. Sci. Mater. Electron. **29**, 17160–17169 (2018)